

Stop-and-go waves reconstruction via iterative refinement

Junyi Ji^{a,b}, Alex Richardson^b, Derek Gloudemans^b, Gergely Zachár^b, Matthew Nice^b, William Barbour^b, Jonathan Sprinkle^{a,b,c}, Benedetto Piccoli^d, Daniel B. Work^{a,b,c}

^a*Department of Civil and Environmental Engineering, Vanderbilt University, United States*

^b*Institute for Software Integrated Systems, Vanderbilt University, United States*

^c*Department of Computer Science, Vanderbilt University, United States*

^d*Department of Mathematical Sciences, Rutgers University–Camden, United States*

Abstract

Stop-and-go waves are a fundamental phenomenon in freeway traffic flow, contributing to inefficiencies, crashes, and emissions. Recent advancements in high-fidelity sensor technologies have improved the ability to capture detailed traffic dynamics, yet such systems remain scarce and costly. In contrast, conventional traffic sensors are widely deployed but suffer from relatively coarse-grain data resolution, potentially impeding accurate analysis of stop-and-go waves. This article explores whether generative AI models can enhance the resolution of conventional traffic sensor to approximate the quality of high-fidelity observations. We present a novel approach using a conditional diffusion denoising model, designed to reconstruct fine-grained traffic speed field from radar-based conventional sensors via iterative refinement. We introduce a new dataset, I24-WaveX, comprising 132 hours of data from both low and high-fidelity sensor systems, totaling over 2 million vehicle miles traveled. Our approach leverages this dataset to formulate the traffic measurement enhancement problem as a spatio-temporal super-resolution task. We demonstrate that our model can effectively reproduce the patterns of stop-and-go waves, achieving high accuracy in capturing these critical traffic dynamics. Our results show promising advancements in traffic data enhancement, offering a cost-effective way to leverage existing low spatio-temporal resolution sensor networks for improved traffic analysis and management. We also open-sourced our trained model and code to facilitate further research and applications.

Keywords: stop-and-go waves, super resolution, generative artificial intelligence, diffusion model

1. Introduction

Stop-and-go waves are among the most ubiquitous and significant phenomena in freeway traffic flow research [1; 2; 3]. Stop-and-go waves have been recognized as a major contributor to the system inefficiencies, crashes [4] and emissions [5; 6].

Modern freeway *traffic management centers* (TMCs) commonly utilize sensors such as loop detectors [7] and radar detectors [8] in daily operations to implement various corridor management strategies [9]. These sensors typically provide aggregated traffic measurements at typical intervals of 30 seconds to 5 minutes and are usually deployed at 0.5 to 1-mile intervals along the freeway. Because of such sensors, we know that stop-and-go traffic waves are extremely prevalent in freeway corridors [10]. However, while radar and inductive loop sensors offer a good cost-benefit ratio compared to expensive high-fidelity sensors for TMCs, their lack of fine

Email address: junyi.ji@vanderbilt.edu (Junyi Ji)

spatio-temporal resolution means that they cannot accurately measure periods of low-speed travel temporally close to periods of high-speed travel [11; 12]. This underestimation is particularly problematic as these low-speed parts are critical for accurately estimating stop-and-go wave characteristics.

In recent years, advanced sensor technologies such as drones [13; 14], multi-camera monitoring systems [15; 16], LiDAR [17; 18], and on-board vehicle perception systems [19] have allowed the collection of precise vehicle trajectories, which has enabled rapid advancement in the analysis and modeling of stop-and-go waves [20; 21; 22; 16]. High-fidelity traffic measurements have demonstrated the capability to capture the intricate patterns of stop-and-go waves, which exhibit considerable complexity, as shown in [23; 24]. Figure 1 demonstrates a comparison of the traffic speed profiles observed from a conventional sensor system and high-fidelity sensor systems. Unfortunately, very few roadways worldwide currently have access to high-fidelity traffic instruments mentioned above capable of continuously collecting extensive vehicle trajectory data [25]. This significantly limits the generalizability and scalability of the observation and analysis of stop-and-go traffic to a broader context.

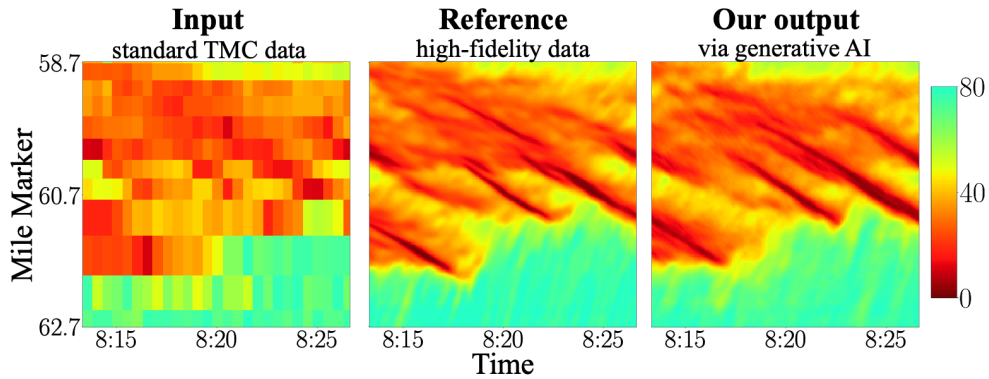


Figure 1: Stop-and-go waves observed from a standard traffic sensor system (left), a high-fidelity sensor system (middle), and a generative model output (right) using the low spatio-temporal resolution data as input. The examples used here are extracted from Interstate 24 near Nashville, Tennessee in the United States, dated June 3rd, 2024 during the morning peak hours. In these examples, the x-axis represents the local time, and the y-axis represents the mile marker of the freeway. The high-fidelity sensors distinctly highlight the stop-and-go wave patterns, providing a much clearer and detailed view of the traffic flow dynamics.

Recent years have seen a flurry of advancements in generative artificial intelligence (AI) models, and their diverse applications [26; 27] have leveraged the potential of large-scale data via generative models, motivating the primary thesis of this work: **generative models can learn the underlying mechanisms of traffic from low spatio-temporal resolution sensor input to generate enhanced data which better capturing stop-and-go waves, almost to the resolution of high-fidelity traffic sensors.**

To investigate this, we collected 132 hours of rush-hour traffic data over 49 days from a stretch of 4 miles of roadway, amounting to over 2 million vehicle miles traveled (VMT). The dataset, named I24-WaveX, was gathered simultaneously from two distinct sensor systems: one from a commonly used freeway radar detector system (with sensors deployed every 0.3 to 0.5 mile and aggregated every 30 seconds), and the other from a camera-based traffic testbed capable of capturing individual vehicle trajectories (aggregated into speed profile data with bin resolution of 4 seconds and 0.02 miles, approximately 32 meters) [16; 28]. We then formulated the data enhancement problem as a traffic measurement super-resolution reconstruction task, with the goal of reconstructing the higher-fidelity data using only the lower fidelity data as input. To this end, we implemented a conditional diffusion denoising model for iterative refinement. Finally,

we evaluated the extent to which our proposed method accurately reconstructs the details of stop-and-go waves.

The contributions of this paper are:

- (1) We are the first to apply a generative conditional diffusion denoising model designed to improve the spatio-temporal resolution of traditional freeway roadside traffic sensors, addressing the traffic measurement super-resolution challenge.
- (2) We produce the I24-WaveX dataset, a new large-scale empirical dataset over 2 million vehicle miles traveled featuring stop-and-go traffic, which was collected concurrently using both high-resolution and low-resolution sensor systems over 49 days, 4 to 4.5 hours a day. This dataset is intended to investigate the potential of generative models in analyzing traffic flow.
- (3) We demonstrate that our model can reproduce wave properties, effectively capturing the complex details of stop-and-go traffic patterns and significantly outperforming existing methods across a variety of metrics.
- (4) We release the code and fine-trained model parameters trained on the data to enhance the reproducibility of this paper future research.

The rest of this article is organized as follows: first, we briefly discuss related work on traffic waves and applications of generative models to traffic. We then describe the method proposed in this work, Next we illustrate the data collected and the experiments used to validate our methods, and present the obtained results. The article concludes with a discussion on the ability of the method to capture fine-grained wave properties and its limitations.

2. Related work and challenges

Traffic reconstruction across all scales [29] requires data collection as the first step. Efforts in empirical traffic data collection have been ongoing since 1933 [30], and these efforts can be categorized into *microscopic* and *macroscopic* scales. Macroscopic traffic data [30; 31; 32; 10; 33; 8], which refers to the aggregated traffic measurements typically collected from loop detectors, provides insights into collective phenomena such as the fundamental diagram and capacity drop [34; 35] On the other hand, microscopic traffic data such as vehicle trajectory data in a common reference system[36; 21], helps researchers understand individual vehicle behaviors.

Traffic data which captures observations of both microscopic and macroscopic phenomena has significant value in the transportation research community. A relative scarcity of these data has limited empirical validation of theory in individual dynamics and traffic system dynamics. To date, only a few datasets are available which capture both microscopic and macroscopic data. Data collected from mobile and fixed sensors by the Mobile Century experiments [37] have been utilized for traffic reconstruction. Additionally, INRIX and loop detector data [12] have been collected and employed for cross-validation purposes. Purveyors of GPS-navigation applications have vehicle trajectory and aggregate data, but these are proprietary. Further efforts and contributions are needed to expand the availability and diversity of datasets in this field.

Ideally, microscopic and macroscopic scales in traffic measurement could be converted into another, similar to the concept of downsampling and upsampling in image processing [38]. In practice, transitioning from microscopic to macroscopic is straightforward through aggregation via Edie’s definition [2], whereas transforming from macroscopic to microscopic is more challenging due to the complex and heterogeneous dynamics of individual particles in the traffic flow system. The problem is often referred to as *traffic reconstruction* [37; 39; 40]. One paradigm from previous research involves calibrating sets of microscopic modelled driving behaviors to

replicate macroscopic measurements or phenomena [41]. A limitation of using micro-simulation to reproduce macroscopic phenomena is the inherent mismatch between the model and real-world aggregated data, which may not fully capture the complex and dynamic nature of actual traffic systems [42; 39]. Another paradigm involves using kernel smoothing [43; 44] and similar techniques to interpolate and impute sparse observations, in order to enhance the resolution and completeness of traffic data by filling in gaps and smoothing out inconsistencies. The adaptive smoothing method [45; 43; 46] is a widely recognized approach in this direction. More recently, the refinement problem was proposed and defined by [47], which utilized a simple linear regression approach that accounts for different traffic states to enhance traffic measurement resolution. The method proposed in that study achieves a 2 by 2 lift in resolution for both space and time each time, demonstrating the potential to improve resolution from 200 meters by 60 seconds to 50 meters by 30 seconds. In other fluid dynamical systems, deep learning has been explored and applied to the reconstruction problem. These approaches have shown promise in accurately capturing and reconstructing complex fluid dynamics [48; 49; 50], suggesting potential applicability to traffic flow systems [51] as well.

In recent years, the field of image processing has seen significant advancements due to generative artificial intelligence. Generative models have enabled the transformation of low-resolution images into high-resolution ones via a process known as *super-resolution* [52]. This aligns well with the problem of enhancing traffic measurement resolution. The concept of generative deep learning gained prominence with the introduction of generative adversarial networks (GANs) [53], which have been extensively applied in traffic systems for tasks such as traffic data imputation [54; 55] and traffic state estimation [56]. More recently, diffusion probabilistic models have emerged as a promising approach [27]. These models have been investigated for tasks such as noisy data recovery [57] and GPS trajectory data generation [58], demonstrating their robustness to hyperparameters and their potential for a wide range of applications. These advancements in generative diffusion models offer new opportunities for improving traffic measurement resolution and addressing the challenges associated with low spatio-temporal resolution data, which have not been investigated before.

3. Methodology

3.1. Problem formulation

In this article, stop-and-go wave enhancement refers to the problem of recovering fine-grained speed data (high-fidelity) from corresponding coarse-grained traffic measurement data (relatively low-fidelity), which can be viewed as a super-resolution task. *Coarse-grained data* typically collected from radar detectors or loop detectors, is considered low spatio-temporal resolution data and is denoted by $\mathbf{r} \in \mathcal{R}$. *Fine-grained speed data*, generated from vehicle trajectory data, is viewed as high-fidelity data and is represented by $\mathbf{m} \in \mathcal{M}$. For a given space and time range, forming tensors \mathbf{r} and \mathbf{m} herein, each observation of coarse-grained data is represented as $\mathbf{r} \in \mathbb{R}^{T_r \times S_r \times 3}$ and fine-grained data is represented as $\mathbf{m} \in \mathbb{R}^{T_m \times S_m \times 1}$, where T_r , S_r , T_m , S_m are the number of time and space observations in the space-time range, respectively. Typically, $T_r < T_m$ and $S_r < S_m$, which induces a dimension lifting in the output. The coarse-grained data contains three traffic measurements: speed, volume, and occupancy, whereas the fine-grained data includes only one measurement: speed. The problem addressed in this context is to find a mapping function $f : \mathcal{R} \rightarrow \mathcal{M}$ that can restore the fine-scale details of stop-and-go waves in traffic from the coarse-grained data.

3.2. Conditional denoising diffusion model

The conditional denoising diffusion model is proposed by [59] to address the image super resolution tasks, and we apply this method here. Given a dataset consisting of input-output

pairs of coarse-grained and fine-grained data, denoted as $\mathcal{D} = \{\mathcal{R}, \mathcal{M}\}$, which are samples from an unknown conditional distribution $p(\mathcal{M} | \mathcal{R})$, our objective is to learn a parametric approximation of $p(\mathcal{M} | \mathcal{R})$. This is achieved through a stochastic iterative refinement process that maps a coarse-grained traffic observation to a target fine-grained speed field.

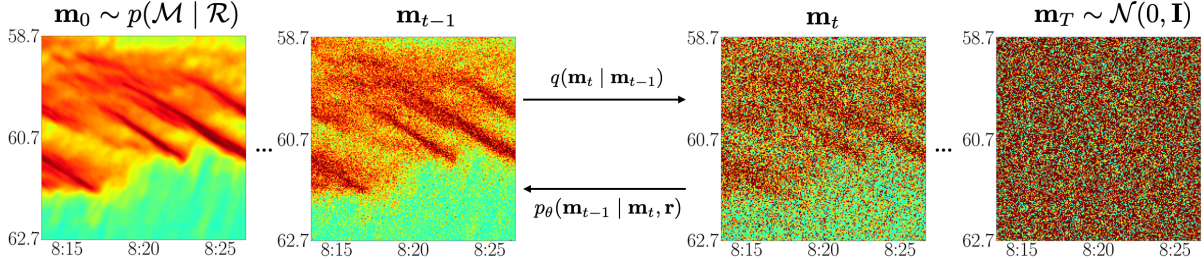


Figure 2: Demonstration of the forward (left to right) and inverse (right to left) diffusion process in our problem. Noted that the coarse-grained data is not shown here; refer to Figure 1 for the input speed profile of \mathbf{r} .

We adapt the denoising diffusion probabilistic model (DDPM) [59] for conditional fine-grained speed field generation. The method contains a noising process (e.g. forward diffusion) and a denoising process (e.g. inverse diffusion) as shown in Figure 2. These processes are defined as:

Forward diffusion (add noise): the process q gradually adds Gaussian noise over T steps to the fine-grained data $\mathbf{m}_0 = \mathbf{m}$, which can be viewed as a forward Markovian diffusion process.

$$q(\mathbf{m}_{1:T} | \mathbf{m}_0) = \prod_{t=1}^T q(\mathbf{m}_t | \mathbf{m}_{t-1}) \quad (1)$$

$$q(\mathbf{m}_t | \mathbf{m}_{t-1}) = \mathcal{N}(\mathbf{m}_t | \sqrt{\alpha_t} \mathbf{m}_{t-1}, (1 - \alpha_t) \mathbf{I}) \quad (2)$$

Here, the scalar parameters $\alpha_{1:T}$ are hyper-parameters where $0 < \alpha_t < 1$, which determine the variance of the noise added at each iteration t . For each step, the distribution of \mathbf{m}_t given by \mathbf{m}_0 can be expressed as:

$$q(\mathbf{m}_t | \mathbf{m}_0) = \mathcal{N}(\mathbf{m}_t | \sqrt{\gamma_t} \mathbf{m}_0, (1 - \gamma_t) \mathbf{I}), \quad (3)$$

where $\gamma_t = \prod_{i=1}^t \alpha_i$.

Learn the inverse diffusion (denoise): to reverse the forward diffusion process, a neural denoising model f_θ takes the coarse-grained data \mathbf{r} and the noisy target image $\tilde{\mathbf{m}}$ as defined in Equation 3,

$$\tilde{\mathbf{m}} = \sqrt{\gamma} \mathbf{m}_0 + \sqrt{1 - \gamma} \epsilon, \quad \epsilon \in \mathcal{N}(0, \mathbf{I}) \quad (4)$$

The model $f_\theta(\mathbf{r}, \tilde{\mathbf{m}}, \gamma)$ is trying to learn from the coarse data \mathbf{r} , the noisy target image $\tilde{\mathbf{m}}$, as well as the variance of the noise γ , to predict the noise vector ϵ in Equation 4. Here, γ is the scalar parameter drawn from the distribution $p(\gamma)$. The objective function for training f_θ is written as:

$$\mathbb{E}_{(\mathbf{r}, \mathbf{m})} \mathbb{E}_{\epsilon, \gamma} \left\| f_\theta \left(\mathbf{r}, \underbrace{\sqrt{\gamma} \mathbf{m}_0 + \sqrt{1 - \gamma} \epsilon}_{\tilde{\mathbf{m}}}, \gamma \right) - \epsilon \right\|_2^2. \quad (5)$$

During the training process, each iteration takes a gradient descent step:

$$\nabla_\theta \left\| f_\theta(\mathbf{r}, \sqrt{\gamma} \mathbf{m}_0 + \sqrt{1 - \gamma} \epsilon, \gamma) - \epsilon \right\|_2^2 \quad (6)$$

until convergence. The detailed proof and justification of the choice of the objective function for f_θ from the perspective of a variational lower bound and denoising score-matching can be found in [27; 59].

Note that the model is learning the output of f_θ to the Gaussian noise, not the \mathbf{m}_0 . As a result, it is not feasible to use the typical tricks to get physics informed learning [60]. To address this, we design a weighting function $\mathbf{W}(\mathbf{m}, v_c)$ for the loss to focus on the areas of interest, which, in our problem, are the stop-and-go waves. The weighting function is written as:

$$\mathbf{W}_{ij}(\mathbf{r}, v_c) = \begin{cases} \omega & \text{if } \mathbf{m}_{ij} < v_c \\ 1 - \omega & \text{if } \mathbf{m}_{ij} \geq v_c \end{cases}, \quad (7)$$

where ω and v_c is the hyperparameter, \mathbf{m}_{ij} denotes the value at time index i and space index j in the fine-grained speed data. The weighting matrix is subsequently integrated into the training process. The weighted gradient descent step during training is defined as:

$$\nabla_\theta \left\| \mathbf{W} \odot (f_\theta(\mathbf{r}, \sqrt{\gamma}\mathbf{m}_0 + \sqrt{1-\gamma}\epsilon, \gamma) - \epsilon) \right\|_2^2, \quad (8)$$

where \odot denotes element-wise multiplication.

Inference via iterative refinement: The reverse inference process p iteratively denoises the noisy data using conditioned on the input coarse-grained data \mathbf{r} . Starting with purely Gaussian noise $\mathbf{m}_T \sim \mathcal{N}(0, \mathbf{I})$ and the corresponding coarse-grained data \mathbf{r} , the model iteratively refines the speed field through successive iterations $(\mathbf{m}_{T-1}, \dots, \mathbf{m}_t, \mathbf{m}_{t-1}, \dots, \mathbf{m}_0)$ according to the learned conditional transition distribution:

$$\mathbf{m}_{t-1} = \frac{1}{\sqrt{\alpha_t}} \left(\mathbf{m}_t - \frac{1 - \alpha_t}{\sqrt{1 - \gamma_t}} f_\theta(\mathbf{r}, \mathbf{m}_t, \gamma_t) \right) + \sqrt{1 - \alpha_t} z, \quad (9)$$

where z is defined as Gaussian noise for all the steps other than $t = 1$ (i.e., $z \sim \mathcal{N}(0, \mathbf{I})$ if $t > 1$, else $z = 0$). The derivation of Equation 9 can be found in [59].

Neural denosing model choice: the UNet [61] architecture is a popular choice for diffusion denoising model regression [27; 59] because its encoder-decoder structure with skip connections effectively captures multi-scale features and preserves high-resolution details throughout the denoising process. Detailed task specific architectural details can be found in the **EXPERIMENTS** section.

4. Data

To address the aforementioned problem, a sufficient amount of high-fidelity data is essential, particularly for training a deep generative model. The data used in this paper is collected from two large-scale traffic measurement systems: a network of millimeter-wave *radar detection systems* (RDS) spanning 17.1 miles at roughly 0.3 to 0.5 mile spacing, and a camera network capable of capturing massive vehicle trajectory data densely covering 4.2 miles of roadway. Each system is detailed below.

4.1. I-24 MOTION data

I-24 MOTION [16] is a traffic instrument located along 4.2 miles of interstate roadway near Nashville, Tennessee. It consists of 276 4k-resolution cameras mounted on 40 110-foot tall traffic poles, sufficient to densely survey this portion of roadway. Computer vision detection

and tracking algorithms [62] are applied to the video data to produce vehicle trajectories for vehicles travelling through the roadway.

Trajectory data produced by I-24 MOTION was used to create fine-grained *mean speed field* data for this work. A selection of 33 days were selected, recorded from May 17 to July 17, 2024; for each day the morning rush hour period (6:00 or 5:30 AM to 10:00 AM) was considered as this period has the most dynamic and variable traffic conditions. Figure 3 shows the raw trajectory data for each selected day. The selected trajectory data was then sampled to create a fine-grained mean speed field with 4 second and 0.02 mile bin resolution. For cells with no data and cells with inconsistent values, speed was interpolated using an adaptive smoothing method [43; 28], with parameters shown in Table 2.

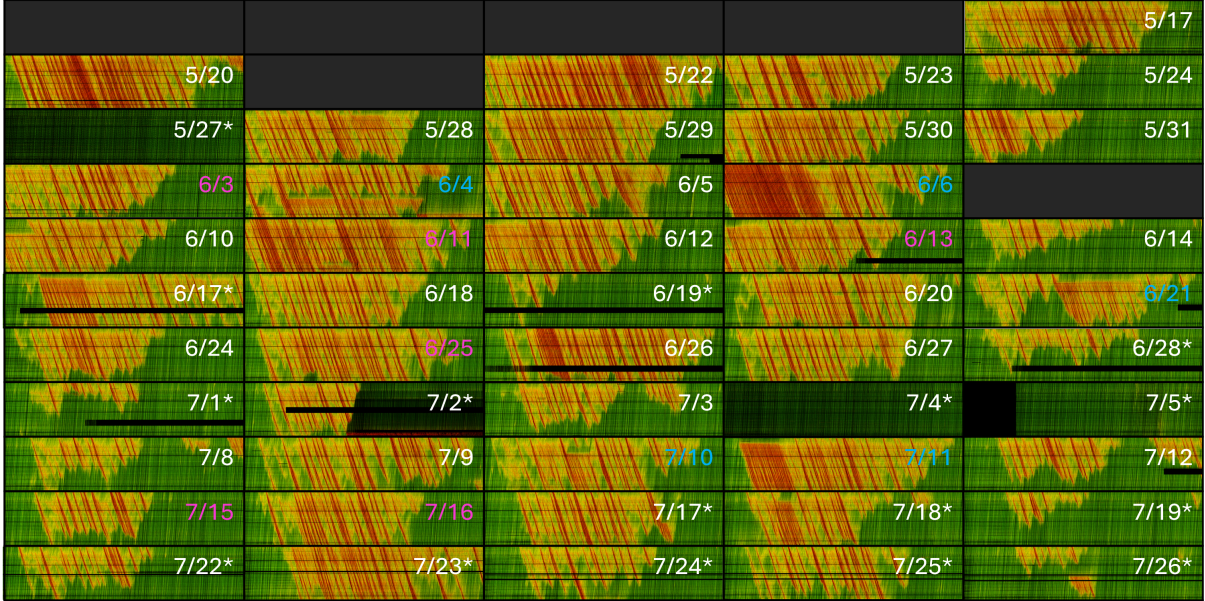


Figure 3: Time-space trajectory data diagrams for each included day in the I-24 MOTION: WaveX dataset. Each day of data spans 4.2 miles (y-axis) and 4 hours (x-axis) and is produced with ~ 2 -foot positional accuracy and at 10Hz. Days with no data due to e.g. system maintenance are filled with dark grey. (pink text) validation holdout days. (blue text) testing holdout (notable event) days. Days with an asterisk were not used in model training and evaluation due to missing data or other anomalous events, but are released with the dataset.

Table 1: Summary of I-24 MOTION data statistics

	VMT (mile)	VHT (hour)	MS (mph)	Training	Validation	Testing
count				21	7	5
mean	69270	2166	33.2	33.9	34.5	28.6
st.dev.	5486	350	8.0	7.7	9.3	7.2
min	56158	1456	19.8	21.1	22.6	19.8
25%	65445	1941	28.5	29.9	29.5	24.3
50%	70682	2198	31.5	31.5	32.6	27.6
75%	72538	2326	38.0	38.0	38.4	33.2
max	78825	2856	52.4	52.4	50.4	38.1

Table 1 provides an overview of the key metrics in the I-24 MOTION dataset, including Vehicle Miles Traveled (VMT), Vehicle Hours Traveled (VHT), and the mean speed (MS, the

vehicle-miles-weighted speed) [63]. It also outlines the strategy for splitting the data into training and validation sets, with a 75% allocation for training and 25% for validation. Note that the testing set comprises data from 5 days with distinctive congestion patterns due to observable events, which are excluded from both the training and validation sets to avoid model training imbalance.

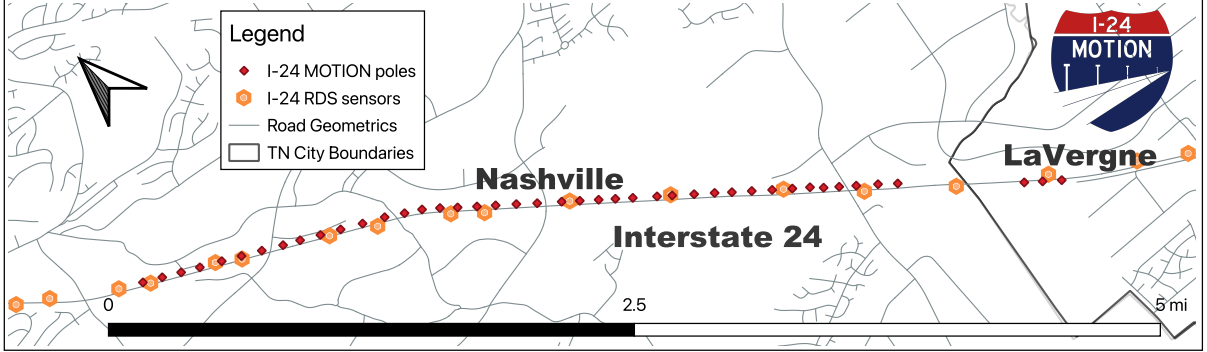


Figure 4: Locations of I-24 MOTION camera poles (which provide complete roadway coverage between) and I-24 RDS sensor placement.

4.2. I-24 RDS data

The I-24 RDS data is obtained from the I-24 radar detection system (RDS) [64; 65]. The system collects lane-level local traffic measurements including speed, occupancy, and volume, aggregated at 30-second intervals. All the radar sensors utilized in this study were meticulously calibrated. For the purposes of this study, we specifically selected the subset of sensors that align spatially with the I-24 MOTION testbed as shown in Figure 4. A total of 11 RDS sensors are aligned in this section. Two additional sensors located at both ends are selected to help with reconstruction.

4.3. Dataset processing

Pre-processing. To address the sparsity of I-24 RDS data at higher space-time resolutions, we utilize the adaptive smoothing method [43]. This widely-used upsampling strategy for traffic measurements lifts the dimensionality of the RDS data to match that of I-24 MOTION, specifically to $\mathbb{R}^{T_m \times S_m \times 3}$, denoted as $\tilde{\mathbf{r}}$. The adaptive smoothing method produces a complete matrix, which is then used as input data for training and validation. Parameters used in the adaptive smoothing method is listed in Table 2 In this paper, both S_m and T_m are set to 200, corresponding to a spatio-temporal tensor spanning 800 seconds and 4 miles. In this paper, experiments and discussions are exclusively based on data from lane 1 (the leftmost lane) and the high-occupancy vehicle (HOV) lane for both the I-24 MOTION and I-24 RDS data.

Table 2: Parameters of the adaptive smoothing method

	Meaning	I-24 MOTION	I-24 RDS
σ (mile)	smoothing width in time coordinate	0.12	1
τ (second)	smoothing width in space coordinate	20	60
c_{free} (mph)	wave speed in free traffic	-12.5	-13.0
c_{cong} (mph)	wave speed in congested traffic	60.0	60.0
V_{thr} (mph)	crossover from congested to free traffic	37.29	37.29
ΔV (mph)	transition width between congested and free traffic	12.43	12.43

Dataset augmentation. To augment the dataset, we employed a sliding window strategy, generating multiple overlapping sub-datasets from the original daily dataset matrix. Starting with an original tensor of size 3600×200 , we created multiple 200×200 sub-tensors. A 200×200 window slides across the larger matrix with a defined step size, producing a new 200×200 tensor at each step. In this study, we used a sliding window step size of 10, corresponding to 40 seconds in time. For the validation part, the augmentation via sliding window is not used.

4.4. Data Availability

All days of I-24 MOTION mean speed field data, as well as all corresponding days of I-24 RDS data, will be made available at i24motion.org.

5. Experiments

5.1. Task specific architectural details

In our problem, the coarse-grained data \mathbf{r} is preprocessed with upsampling to be $\tilde{\mathbf{r}}$ (as shown in Figure 5) is concatenated with the noisy fine-grained speed data \mathbf{m}_t . This process generates a 4-channel tensor as the model input, while the model output is a single-channel tensor \mathbf{m}_{t-1} . The UNet [61] architecture employed in this paper comprises an initial level with 64 channels, followed by levels with 128, 256, and 512 channels, culminating in a bottleneck level with 1024 channels, as shown in Figure 5. Each block within this architecture consists of three convolutional ResNet blocks augmented with a multi-head attention mechanism, leading to a total of 130 million trainable parameters.

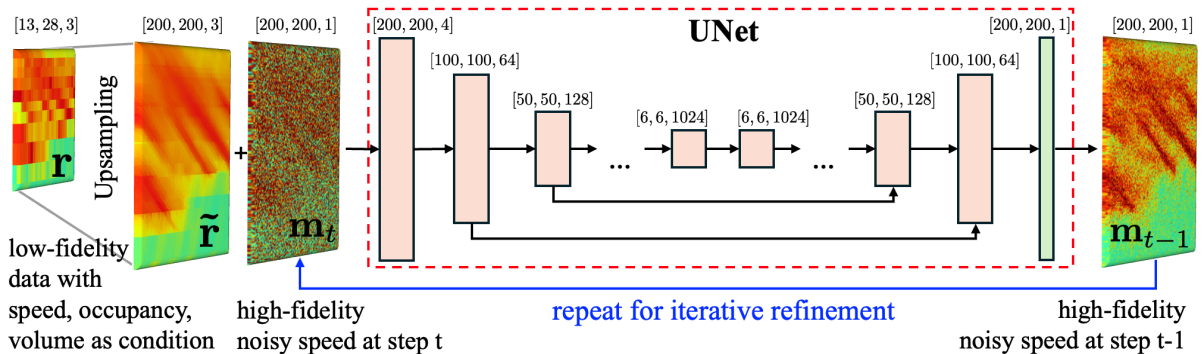


Figure 5: The UNet architecture iteratively refines the denoising process by concatenating the output from the previous step \mathbf{m}_t with the upsampled low spatio-temporal resolution data $\tilde{\mathbf{r}}$. This process is conditioned on speed, occupancy, and volume of the low spatio-temporal resolution data. The specific UNet architecture employed for our tasks is depicted in the middle of the figure.

In this paper, we define a sequence of γ values, which are essential for our diffusion process. These values are uniformly distributed with $p(\gamma)$ within a specified range for T steps, starting from $\gamma_{\text{start}} = 0.001$ to $\gamma_{\text{end}} = 0.02$. The total number of values in this sequence is equal to the number of time steps, $T = 500$, in our diffusion process. The learning rate for the optimizer of the neural denoising model is set at 2×10^{-4} . The velocity v_c is set to 16 mph, and the parameter ω is set to 0.8. An early stopping strategy is employed when the validation loss begins to increase. The best performance on the validation dataset is retained for inference purposes.

5.2. Benchmarked methods

For the purpose of comparison, several methods evaluated on the formulated problem:

- (1) **Average:** missing data points are imputed as the average of all available data points, assuming the data is uniformly distributed in space and time.
- (2) **Nearest:** fills in missing data points by assigning the value of the nearest available data point.
- (3) **Linear:** linear interpolation of missing data points (interpolation is carried out across the time dimension first, then the space dimension).
- (4) **Adaptive smoothing method (ASM) [43]:** interpolates and smooths the values using two different smoothing kernels: one for free-flowing traffic and the other for congested traffic. The results are then combined using a tanh activation function.
- (5) **Ours:** the generative model with iterative refinement proposed in this paper.

5.3. Code and tools

The model is coded using PyTorch, leveraging CUDA for accelerated computation. All experiments are performed on a machine with two NVIDIA RTX A6000 GPUs. The code is open-sourced and available at i24motion.org, facilitating future research and enabling other researchers to build upon our work.

5.4. Evaluation Metrics

The following metrics were used to evaluate the benchmarked methods:

- (1) *Wasserstein distance* (WD) [66]: The Wasserstein distance quantifies the difference between two probability distributions. A smaller distance suggests that the distribution is more closely aligned with the reference distribution.
- (2) *Root mean squared error* (RMSE): in miles per hour
- (3) *Mean absolute percentage error* (MAPE): as a percentage of the true speed

Table 3: Evaluation matrices on different data refinement methods and our improvements over the second best method

Metric	Average	Nearest	Linear	ASM	Ours	Improvement
Training						
WD	20.74	1.92	2.82	3.08	1.24	35.42%
RMSE	23.19	9.36	7.87	7.38	5.38	27.10%
MAPE	1.37	0.47	0.48	0.41	0.16	60.98%
Validation						
WD	20.35	1.97	2.86	3.12	1.38	29.95%
RMSE	22.77	9.56	8.11	8.05	6.81	15.40%
MAPE	1.33	0.49	0.49	0.43	0.28	29.95%
Testing						
WD	19.39	1.81	2.67	3.18	1.59	12.15%
RMSE	21.98	9.88	8.31	7.87	7.17	8.89%
MAPE	1.41	0.54	0.54	0.48	0.32	33.33%

6. Results and discussions

6.1. Overall performance

Table 3 presents a detailed evaluation comparing the performance of our method with various baselines. The results clearly indicate that our method outperforms the baseline methods across all evaluation metrics and datasets. Notably, the superior performance of our method in minimizing the *Wasserstein Distance* (WD), 35.42% in training, 29.95% in validation and 12.15% in testing over the second-best methods, underscores its efficacy in accurately reconstructing speed distributions, which is crucial for stop-and-go wave reconstruction. The substantial improvement in the WD metric suggests that our method captures the correct patterns, even if there are minor spatial misplacement, which is an acceptable limitation as confirmed by the travel time estimates.

In terms of RMSE, our method demonstrates the improvements, with a 27.10% advantage in training, 15.40% in validation, and 8.89% in testing, indicating its robustness in producing refined data with minimal error. The MAPE metric reveals even more pronounced benefits, with our method achieving a 60.98% advantage in training, 34.88% in validation, and 33.33% in testing. These results highlight the overall efficacy of our approach in improving traffic reconstruction across various metrics.

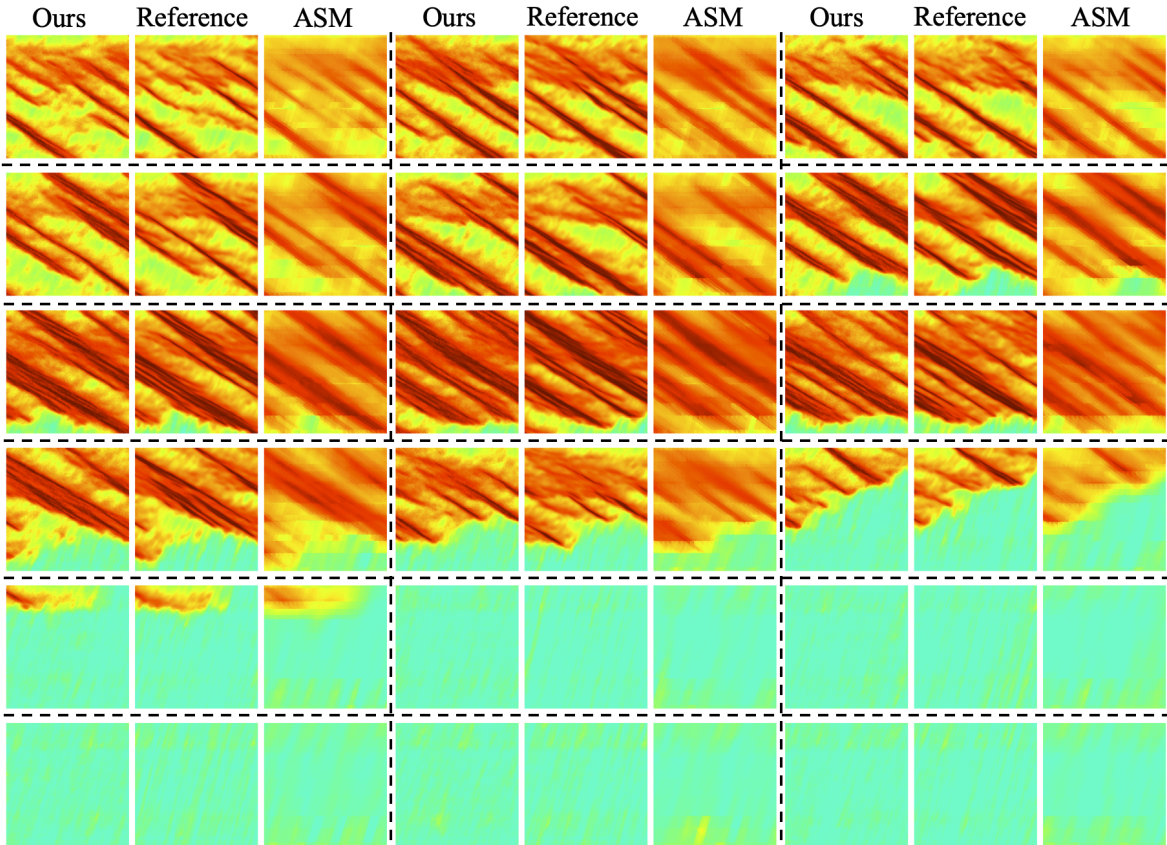


Figure 6: Stop-and-go waves reconstruction on validation data, (June 3, 2024). Each image contains data from 800 seconds (x-axis) and 4 miles (y-axis).

6.2. Congested traffic reconstruction

Figure 7 displays the distribution of the speed profile for the reconstruction from ours (top) and ASM (bottom), with the reference in the middle, on the validation dataset. Note that values outside the 0-80 mph range are clipped to this range. As can be observed from the ASM

reconstruction speed profile distribution, the RDS sensor data with ASM fails to capture the low-speed range, particularly in the 0-10 mph range.

In contrast, our method demonstrates promising reconstruction performance in the low-speed traffic segments, which correspond to stop-and-go traffic conditions. The improved performance in the low-speed range suggests that ours is more effective in reconstructing the intricate patterns of stop-and-go waves, enhancing the overall fidelity of the traffic measurements.

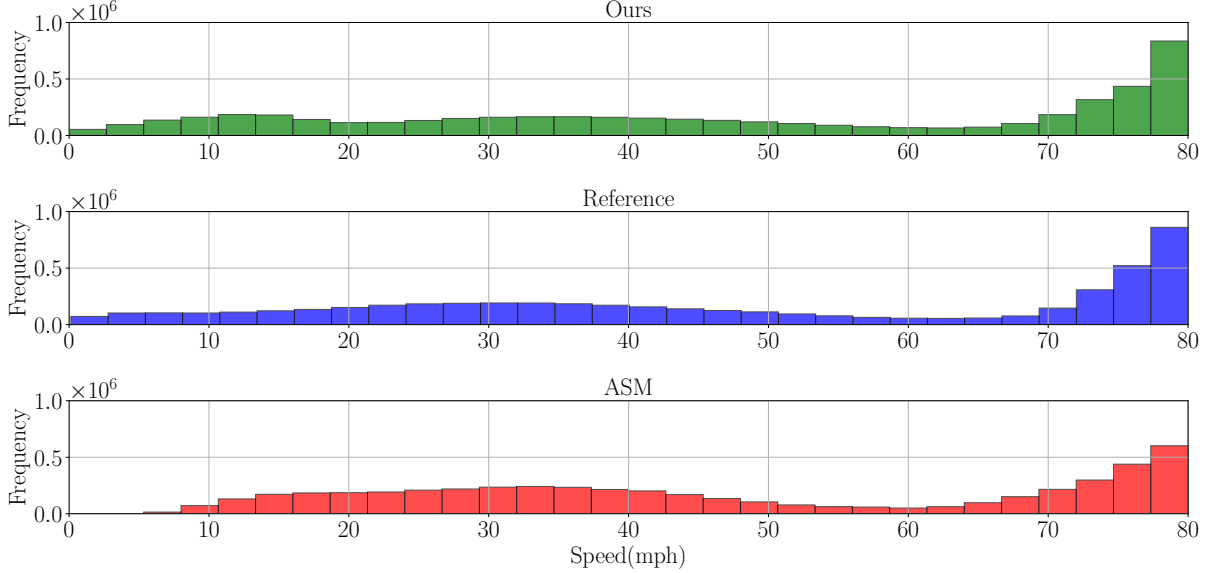


Figure 7: Distribution of accumulated speed profiles: ours (top), reference (middle), ASM (bottom)

6.3. Distribution of errors

Despite the better results compared to baselines of our method indicated by the RMSE and MAPE in Table 3, the errors do not align as closely with the distribution of the speed profile as anticipated. To investigate this discrepancy, we plot the absolute error (shown in Figure 8) on the space-time diagram to analyze the spatio-temporal distribution of our error terms and gain deeper insights into the underlying causes.

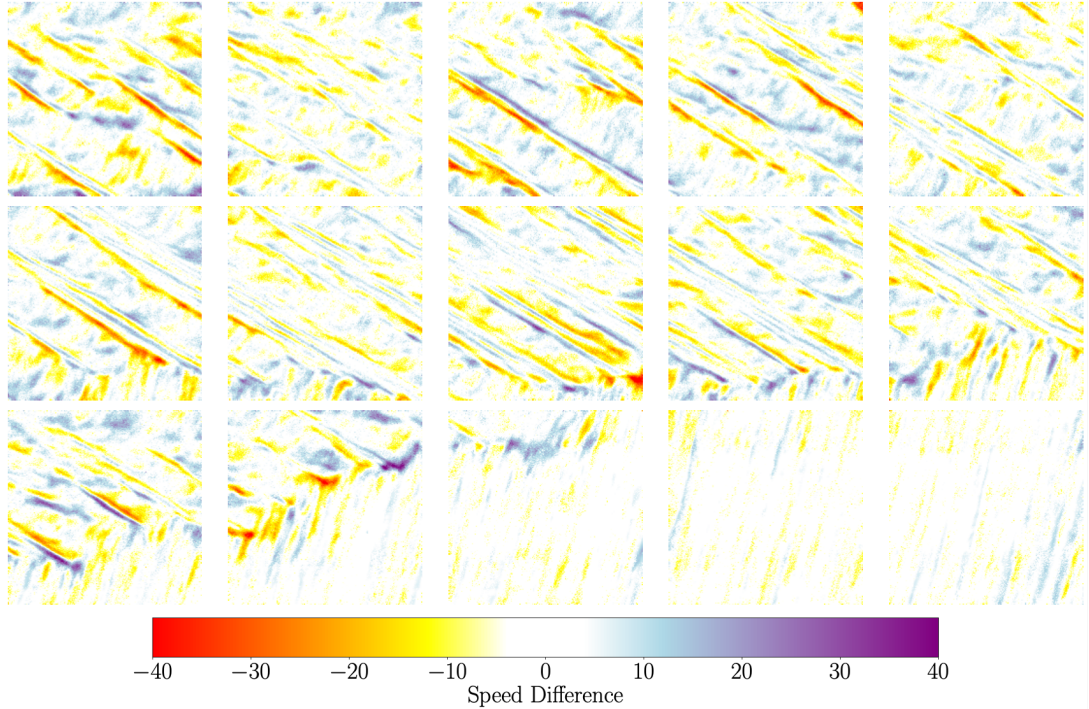


Figure 8: Error distribution plot for the reconstructed speed and the reference speed field, dated on the validation dataset, June 3, 2024

As can be seen in Figure 8, the error terms in speed difference generally exhibit a diagonal pattern, alternating in a faster and slower fashion. This may indicate that the spatio-temporal locations of the stop-and-go waves are mismatched. Specifically, this pattern suggests that the reconstructed data may not accurately align with the true positions and time of the stop-and-go waves. Such mismatches could be due to various factors, including the limitations of the low spatio-temporal resolution data in capturing rapid fluctuations in traffic speed or the inherent challenges in the modeling process. However, we notice that this does not compromise the detection of the “patterns” as confirmed by the high performance with respect to the Wasserstein distance (Table 3).

6.4. Travel time reconstruction

By utilizing the generated speed field, travel time can be estimated through the use of virtual vehicles [67; 28]. For each scenario, a number of vehicles are introduced into the speed field to create virtual trajectories, allowing for the estimation of travel time through these virtual vehicles. In our case, virtual vehicles are deployed into the speed field every 10 seconds, with the corresponding virtual trajectories updated at a frequency of 1Hz.

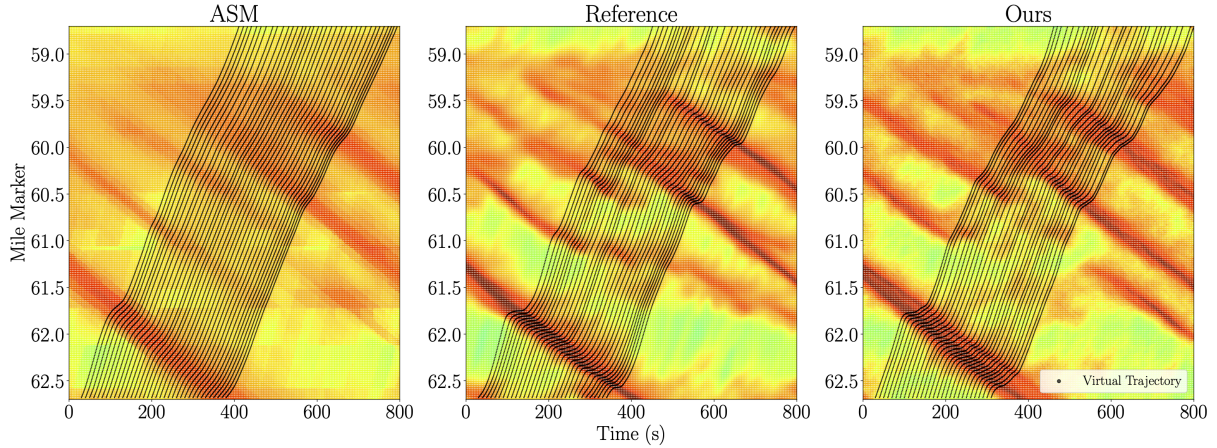


Figure 9: Travel time estimation via virtual trajectories

For the fair comparison, only complete trajectories, in both space and time (as shown in Figure 9), are retained for analysis. This means that only those trajectories with an average speed exceeding 18 mph are considered, given that our generated field spans 4 miles and 800 seconds (the slope of the diagonal is 18 mph). For each speed field, the travel time is estimated by averaging the travel times of all complete virtual trajectories.

Table 4: Statistics on the travel time (in seconds) estimation on the validation dataset

	Reference	ASM	Ours
18-30 mph (37 total)			
mean (seconds)	581.1	509.7	603.9
relative error	-	-12%	+4%
30-50 mph (25 total)			
mean (seconds)	383.9	358.5	387.1
relative error	-	-7%	+1%
50+ mph (43 total)			
mean (seconds)	198.7	201.6	198.8
relative error	-	+1%	+0%

The travel time estimation results across the validation dataset are summarized in Table 4, categorized by the average speed of virtual vehicles into three groups: 18-30 mph, 30-50 mph, and greater than 50 mph. This categorization provides a comprehensive analysis of the performance of our model in different speed ranges.

For the 18-30 mph speed range, which includes a total of 37 samples, the mean travel time estimated by our model is 603.9 seconds with a standard deviation of 89.0 seconds. Compared to the reference mean travel time of 581.1 seconds, our model shows a relative error of +4%, whereas the ASM model exhibits a relative error of -12%. This indicates that while our model slightly overestimates the travel time in this speed range, it does so with reasonable accuracy. In the 30-50 mph speed range, consisting of 25 samples, our model estimates a mean travel time of 387.1 seconds with a standard deviation of 62.5 seconds. The reference mean travel time is 383.9 seconds, resulting in a relative error of +1% for our model. The ASM model, on the other hand, has a relative error of -7%. This suggests that our model performs with high accuracy in this speed range, with minimal deviation from the reference values. The findings suggest that

our model is robust across various speed ranges, especially good in dealing with the challenging stop-and-go traffic conditions.

6.5. Wave speed estimation

We apply the wave analysis tools developed in [24] to validate the wave speed for wave front and tails. Wave fronts are identified as the spatio-temporal points where a virtual vehicle speed drops to 16 mph, while wave tails are defined as the points where the speed increases back above 16 mph.

Table 5: Wave fronts and tails estimated from the speed field

	Reference	ASM	Ours
wave front			
mean speed (mph)	11.97	13.28	13.31
speed st.dev. (mph)	2.10	2.22	2.78
wave tail			
mean speed (mph)	11.51	12.79	12.48
speed st.dev. (mph)	1.89	2.16	2.69

As can be seen from the Table 5, our reconstructed wave speed is very close to the ASM, which is predefined as 13 mph when preprocessing the low spatio-temporal resolution data. A likely cause is the conditional diffusion process on low spatio-temporal resolution data with preprocessing, particularly the upsampling using ASM, which appears to dominate the observed phenomena. This represents a limitation of the current work, necessitating further experiments to explore and mitigate the impact of preprocessing techniques on wave speed estimation.

6.6. Events and crashes

We conducted a manual inspection of all outputs from the validation dataset to identify any apparent errors produced by our models. Figure 10 shows 3 of the typical failed examples in the validation datasets. The initial two rows of the examples indicate that there are crashes/events concealed within the stop-and-go waves. These are not detectable by conventional sensors and, consequently, cannot be retrieved using our methods, which is acceptable. Future research could explore the potential of incorporating event context information into the model as a form of prompt for generation. The final row of the example indicates that data is missing for half of the observation period. The interpolation is degraded by backfilling interpolation, which results in incorrect input and thus inaccurate output. Future research could also investigate whether the generative framework can be useful for data imputation.

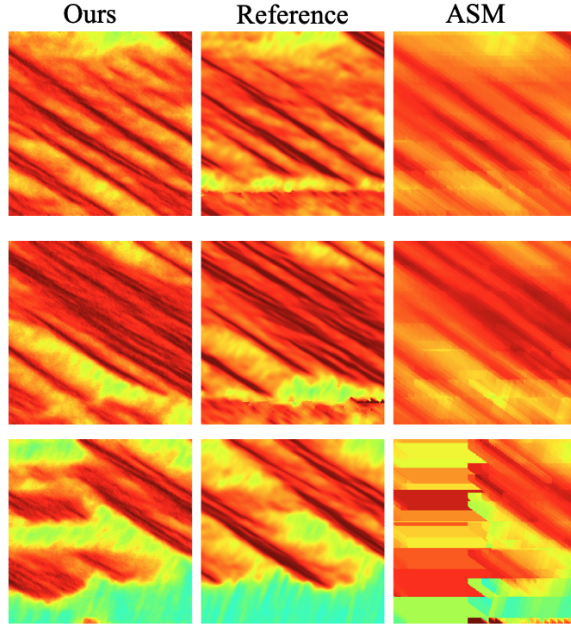


Figure 10: Failed examples in the validation dataset: crashes not observed by the conventional sensor (top and middle), and missing conventional sensor data (bottom).

As shown in Figure 3, the test dataset primarily focuses on crashes and events where the model is expected to struggle. Figure 11 discusses two typical types of crashes in the test dataset. Figure 11(a) illustrates crashes occurring within stop-and-go traffic. The performance of the reconstruction appears satisfactory, particularly when the bottleneck is evident in the conventional sensor data. However, it is clear that the fine-grained details do not align perfectly. Figure 11(b) depicts crashes that cause multiple lane blockages within the observation range, all occurring in slow-moving traffic. It is difficult to discern the wave details due to the lack of similar samples in the training data. These limitations necessitate more quantitative evaluation tools for assessing the generative results. Particularly, crash scenarios require further investigation with more attentions.

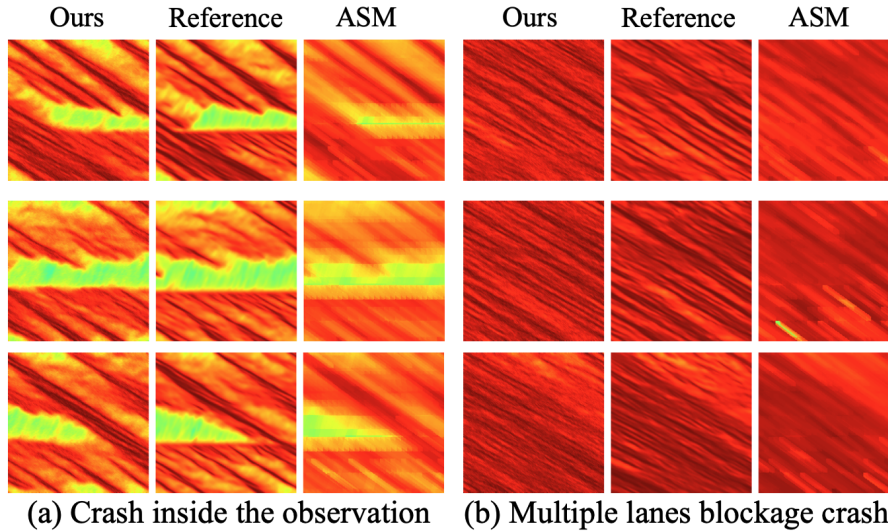


Figure 11: More examples for crash scenarios in the test dataset: (a) crashes inside the stop-and-go traffic, (b) slow traffic under the impact of multiple lanes blockage crashes

7. Conclusion

This paper has demonstrated the potential of generative AI models to enhance the resolution of conventional traffic sensor data, thereby approximating the quality of high-fidelity observations. By employing a conditional diffusion denoising model, we are able to reconstruct fine-grained traffic speed fields from radar-based conventional sensors, effectively addressing the limitations associated with coarse-grain data resolution.

Our proposed approach is validated using a new dataset I24-WaveX which provides a comprehensive ground for testing and comparing our model against various baselines. The results clearly show that our method outperforms the existing techniques across several evaluation metrics, notably in minimizing the Wasserstein Distance (WD) by 29.95% on validation dataset and improving Root Mean Square Error (RMSE) and Mean Absolute Percentage Error (MAPE). Despite spatio-temporal mismatches, our method significantly advances beyond current baseline methods on stop-and-go wave reconstructions by accurately capturing the wave patterns, leading to better estimations of travel times and stop-and-go wave speeds.

However, limitations are also identified, particularly in scenarios involving crashes and complex traffic events, where fine-grained details do not align perfectly with high-fidelity data.

In conclusion, our research contributes to the field of traffic data enhancement by providing a viable method to improve the resolution of conventional traffic sensors. The open-sourcing of our data, trained model and code can also facilitate further research and practical applications with generative AI. Future work will focus on improving our model to address its current limitations, ensuring greater accuracy and reliability in more diverse traffic states.

Acknowledgements

This work was supported by the National Science Foundation (NSF) under Grant No. 2135579 (Work, Sprinkle), and 2111688 (Sprinkle), the U.S. Department of Transportation under Grant No. 693JJ22140000Z44ATNREG3202, and the Tennessee Department of Transportation under Grant No. RES2023-20. It is also supported by the USDOT Dwight D. Eisenhower Fellowship program under Grant Agreement 693JJ32445065 (Richardson). We acknowledge the Tennessee Department of Transportation (TDOT) for providing the data used in this research. We are grateful to Dr. Yanbing Wang from Argonne National Laboratory for her contributions to the I-24 MOTION project. We also appreciate the insights for spatio-temporal modeling from Austin Coursey and Prof. Tyler Derr at Vanderbilt University. The views expressed herein do not necessarily reflect those of the U.S. Department of Transportation, the Tennessee Department of Transportation, or the United States Government.

References

- [1] S. Ahn, B. Coifman, V. Gayah, M. Hadi, S. Hamdar, L. Leclercq, H. Mahmassani, M. Menendez, A. Skabardonis, and H. van Lint, “Traffic flow theory and characteristics,” *Centennial Papers*, 2019.
- [2] L. C. Edie and R. S. Foote, “Experiments on single lane flow in tunnels,” in *Theory of Traffic Flow, Proceedings of the Symposium on the Theory of Traffic Flow* (R. Herman, ed.), (Amsterdam), pp. 175–192, Elsevier Publishing Co., 1961.
- [3] L. C. Edie and E. Baverez, “Generation and propagation of stop-start traffic waves. in vehicular traffic science,” in *Proceedings of the Third International Symposium on the Theory of Traffic Flow Operations Research Society of America*, 1967.
- [4] Z. Zheng, S. Ahn, and C. M. Monsere, “Impact of traffic oscillations on freeway crash occurrences,” *Accident Analysis & Prevention*, vol. 42, no. 2, pp. 626–636, 2010.
- [5] M. Treiber, A. Kesting, and C. Thiemann, “How much does traffic congestion increase fuel consumption and emissions? applying a fuel consumption model to the ngsim trajectory data,” in *87th Annual Meeting of the Transportation Research Board, Washington, DC*, vol. 71, pp. 1–18, 2008.
- [6] X. Li, J. Cui, S. An, and M. Parsafard, “Stop-and-go traffic analysis: Theoretical properties, environmental impacts and oscillation mitigation,” *Transportation Research Part B: Methodological*, vol. 70, pp. 319–339, 2014.
- [7] C. Chen, *Freeway performance measurement system (PeMS)*. PhD thesis, University of California, Berkeley, 2002.
- [8] S. Kim and B. Coifman, “Assessing the performance of speedinfo radar traffic sensors,” *Journal of Intelligent Transportation Systems*, vol. 21, no. 3, pp. 179–189, 2017.
- [9] S. Siri, C. Pasquale, S. Sacone, and A. Ferrara, “Freeway traffic control: A survey,” *Automatica*, vol. 130, p. 109655, 2021.
- [10] M. Treiber, A. Hennecke, and D. Helbing, “Congested traffic states in empirical observations and microscopic simulations,” *Physical review E*, vol. 62, no. 2, p. 1805, 2000.
- [11] B. Coifman, “Improved velocity estimation using single loop detectors,” *Transportation Research Part A: Policy and Practice*, vol. 35, no. 10, pp. 863–880, 2001.

- [12] S. Kim and B. Coifman, “Comparing inrix speed data against concurrent loop detector stations over several months,” *Transportation Research Part C: Emerging Technologies*, vol. 49, pp. 59–72, 2014.
- [13] E. Barmponakis and N. Geroliminis, “On the new era of urban traffic monitoring with massive drone data: The pneuma large-scale field experiment,” *Transportation research part C: emerging technologies*, vol. 111, pp. 50–71, 2020.
- [14] A. Talebpour, H. S. Mahmassani, and S. H. Hamdar, “Third generation simulation data (tgsim): A closer look at the impacts of automated driving systems on human behavior,” Tech. Rep. FHWA-JPO-24-133, University of Illinois at Urbana-Champaign, May 2024. dot:74647.
- [15] X. Shi, D. Zhao, H. Yao, X. Li, D. K. Hale, and A. Ghiasi, “Video-based trajectory extraction with deep learning for high-granularity highway simulation (high-sim),” *Communications in transportation research*, vol. 1, p. 100014, 2021.
- [16] D. Gloudemans, Y. Wang, J. Ji, G. Zachar, W. Barbour, E. Hall, M. Cebelak, L. Smith, and D. B. Work, “I-24 motion: An instrument for freeway traffic science,” *Transportation Research Part C: Emerging Technologies*, vol. 155, p. 104311, 2023.
- [17] H. Lee and B. Coifman, “Using lidar to validate the performance of vehicle classification stations,” *Journal of Intelligent Transportation Systems*, vol. 19, no. 4, pp. 355–369, 2015.
- [18] B. Coifman, M. Wu, K. Redmill, D. A. Thornton, *et al.*, “Segmenting, grouping and tracking vehicles in lidar data,” tech. rep., Nextrans, 2016.
- [19] P. Sun, H. Kretschmar, X. Dotiwalla, A. Chouard, V. Patnaik, P. Tsui, J. Guo, Y. Zhou, Y. Chai, B. Caine, *et al.*, “Scalability in perception for autonomous driving: Waymo open dataset,” in *Proceedings of the IEEE/CVF conference on computer vision and pattern recognition*, pp. 2446–2454, 2020.
- [20] J. Treiterer and J. A. Myers, “The hysteresis phenomenon in traffic flow,” in *Proceedings of the Sixth International Symposium on the Theory of Traffic Flow*, 1974.
- [21] U.S. Department of Transportation Federal Highway Administration, “Next generation simulation (ngsim) vehicle trajectories and supporting data. [dataset]. provided by its datahub through data.transportation.gov,” 2016.
- [22] Hanshin Expressway Co. Ltd., “Zen traffic data.” <https://zen-traffic-data.net>, 2018. Retrieved from Zen Traffic Data.
- [23] J. A. Laval and L. Leclercq, “A mechanism to describe the formation and propagation of stop-and-go waves in congested freeway traffic,” *Philosophical Transactions of the Royal Society A: Mathematical, Physical and Engineering Sciences*, vol. 368, no. 1928, pp. 4519–4541, 2010.
- [24] J. Ji, D. Gloudemans, Y. Wang, G. Zachár, W. Barbour, J. Sprinkle, B. Piccoli, and D. B. Work, “Enabling stop-and-go wave analysis for massive trajectory data,” in *Conference in Emerging Technologies in Transportation Systems (TRC-30)*, (Crete, Greece), September 02–03 2024.
- [25] L. Li, R. Jiang, Z. He, X. M. Chen, and X. Zhou, “Trajectory data-based traffic flow studies: A revisit,” *Transportation Research Part C: Emerging Technologies*, vol. 114, pp. 225–240, 2020.

- [26] T. Brown, B. Mann, N. Ryder, M. Subbiah, J. D. Kaplan, P. Dhariwal, A. Neelakantan, P. Shyam, G. Sastry, A. Askell, *et al.*, “Language models are few-shot learners,” *Advances in neural information processing systems*, vol. 33, pp. 1877–1901, 2020.
- [27] J. Ho, A. Jain, and P. Abbeel, “Denoising diffusion probabilistic models,” *Advances in neural information processing systems*, vol. 33, pp. 6840–6851, 2020.
- [28] J. Ji, Y. Wang, D. Gloudemans, G. Zachár, W. Barbour, and D. B. Work, “Virtual trajectories for i-24 motion: Data and tools,” in *2024 Forum for Innovative Sustainable Transportation Systems (FISTS)*, pp. 1–6, IEEE, 2024.
- [29] B. Piccoli, K. Han, T. L. Friesz, T. Yao, and J. Tang, “Second-order models and traffic data from mobile sensors,” *Transportation Research Part C: Emerging Technologies*, vol. 52, pp. 32–56, 2015.
- [30] B. D. Greenshields, J. Thompson, H. Dickinson, and R. Swinton, *The photographic method of studying traffic behavior*. PhD thesis, note on p. 382., 1933.
- [31] M. J. Cassidy and R. L. Bertini, “Some traffic features at freeway bottlenecks,” *Transportation Research Part B: Methodological*, vol. 33, no. 1, pp. 25–42, 1999.
- [32] C. F. Daganzo, M. J. Cassidy, and R. L. Bertini, “Possible explanations of phase transitions in highway traffic,” *Transportation Research Part A: Policy and Practice*, vol. 33, no. 5, pp. 365–379, 1999.
- [33] B. Coifman, “Estimating travel times and vehicle trajectories on freeways using dual loop detectors,” *Transportation Research Part A: Policy and Practice*, vol. 36, no. 4, pp. 351–364, 2002.
- [34] F. L. Hall and K. Agyemang-Duah, “Freeway capacity drop and the definition of capacity,” *Transportation research record*, no. 1320, 1991.
- [35] K. Chung, J. Rudjanakanoknad, and M. J. Cassidy, “Relation between traffic density and capacity drop at three freeway bottlenecks,” *Transportation Research Part B: Methodological*, vol. 41, no. 1, pp. 82–95, 2007.
- [36] V. G. Kovvali, V. Alexiadis, and L. Zhang PE, “Video-based vehicle trajectory data collection,” tech. rep., Federal Highway Administration, 2007.
- [37] J. C. Herrera and A. M. Bayen, “Traffic flow reconstruction using mobile sensors and loop detector data,” 2007.
- [38] T. Acharya and A. K. Ray, *Image processing: principles and applications*. John Wiley & Sons, 2005.
- [39] M. Montanino and V. Punzo, “Trajectory data reconstruction and simulation-based validation against macroscopic traffic patterns,” *Transportation Research Part B: Methodological*, vol. 80, pp. 82–106, 2015.
- [40] J. Liu, M. Barreau, M. Čičić, and K. H. Johansson, “Learning-based traffic state reconstruction using probe vehicles,” *IFAC-PapersOnLine*, vol. 54, no. 2, pp. 87–92, 2021.
- [41] E. Brockfeld, R. D. Kühne, and P. Wagner, “Calibration and validation of microscopic models of traffic flow,” *Transportation Research Record*, vol. 1934, no. 1, pp. 179–187, 2005.

- [42] V. Punzo, M. Montanino, and B. Ciuffo, “Do we really need to calibrate all the parameters? variance-based sensitivity analysis to simplify microscopic traffic flow models,” *IEEE Transactions on Intelligent Transportation Systems*, vol. 16, no. 1, pp. 184–193, 2014.
- [43] M. Treiber and D. Helbing, “An adaptive smoothing method for traffic state identification from incomplete information,” in *Interface and transport dynamics: Computational Modelling*, pp. 343–360, Springer, 2003.
- [44] E. R. Sanchez, S. Raghavan, and C. Wu, “Data-driven traffic reconstruction and kernel methods for identifying stop-and-go congestion,” *arXiv preprint arXiv:2312.03186*, 2023.
- [45] M. Treiber and D. Helbing, “Reconstructing the spatio-temporal traffic dynamics from stationary detector data,” *Cooperative Transportation Dynamics*, vol. 1, no. 3, pp. 3–1, 2002.
- [46] M. Treiber, A. Kesting, and R. E. Wilson, “Reconstructing the traffic state by fusion of heterogeneous data,” *Computer-Aided Civil and Infrastructure Engineering*, vol. 26, no. 6, pp. 408–419, 2011.
- [47] Z. He, “Refining time-space traffic diagrams: A simple multiple linear regression model,” *IEEE Transactions on Intelligent Transportation Systems*, 2023.
- [48] K. Fukami, K. Fukagata, and K. Taira, “Super-resolution reconstruction of turbulent flows with machine learning,” *Journal of Fluid Mechanics*, vol. 870, pp. 106–120, 2019.
- [49] M. Yoda, “Super-resolution imaging in fluid mechanics using new illumination approaches,” *Annual Review of Fluid Mechanics*, vol. 52, no. 1, pp. 369–393, 2020.
- [50] Z. Wang, X. Li, L. Liu, X. Wu, P. Hao, X. Zhang, and F. He, “Deep-learning-based super-resolution reconstruction of high-speed imaging in fluids,” *Physics of Fluids*, vol. 34, no. 3, 2022.
- [51] V. Morand, N. Müller, R. Weightman, B. Piccoli, A. Keimer, and A. M. Bayen, “Deep learning of first-order nonlinear hyperbolic conservation law solvers,” *Journal of Computational Physics*, vol. 511, p. 113114, 2024.
- [52] S. C. Park, M. K. Park, and M. G. Kang, “Super-resolution image reconstruction: a technical overview,” *IEEE signal processing magazine*, vol. 20, no. 3, pp. 21–36, 2003.
- [53] I. Goodfellow, J. Pouget-Abadie, M. Mirza, B. Xu, D. Warde-Farley, S. Ozair, A. Courville, and Y. Bengio, “Generative adversarial networks,” *Communications of the ACM*, vol. 63, no. 11, pp. 139–144, 2020.
- [54] Y. Chen, Y. Lv, and F.-Y. Wang, “Traffic flow imputation using parallel data and generative adversarial networks,” *IEEE Transactions on Intelligent Transportation Systems*, vol. 21, no. 4, pp. 1624–1630, 2019.
- [55] W. Zhang, P. Zhang, Y. Yu, X. Li, S. A. Biancardo, and J. Zhang, “Missing data repairs for traffic flow with self-attention generative adversarial imputation net,” *IEEE Transactions on Intelligent Transportation Systems*, vol. 23, no. 7, pp. 7919–7930, 2021.
- [56] Z. Mo, Y. Fu, D. Xu, and X. Di, “Trafficflowgan: Physics-informed flow based generative adversarial network for uncertainty quantification,” in *Joint European Conference on Machine Learning and Knowledge Discovery in Databases*, pp. 323–339, Springer, 2022.

- [57] Z. Zheng, Z. Wang, Z. Hu, Z. Wan, and W. Ma, “Recovering traffic data from the corrupted noise: A doubly physics-regularized denoising diffusion model,” *Transportation Research Part C: Emerging Technologies*, vol. 160, p. 104513, 2024.
- [58] Z. Zhong, D. Rempe, D. Xu, Y. Chen, S. Veer, T. Che, B. Ray, and M. Pavone, “Guided conditional diffusion for controllable traffic simulation,” in *2023 IEEE International Conference on Robotics and Automation (ICRA)*, pp. 3560–3566, IEEE, 2023.
- [59] C. Saharia, J. Ho, W. Chan, T. Salimans, D. J. Fleet, and M. Norouzi, “Image super-resolution via iterative refinement,” *IEEE transactions on pattern analysis and machine intelligence*, vol. 45, no. 4, pp. 4713–4726, 2022.
- [60] S. Cai, Z. Mao, Z. Wang, M. Yin, and G. E. Karniadakis, “Physics-informed neural networks (pinns) for fluid mechanics: A review,” *Acta Mechanica Sinica*, vol. 37, no. 12, pp. 1727–1738, 2021.
- [61] O. Ronneberger, P. Fischer, and T. Brox, “U-net: Convolutional networks for biomedical image segmentation,” in *Medical image computing and computer-assisted intervention—MICCAI 2015: 18th international conference, Munich, Germany, October 5–9, 2015, proceedings, part III 18*, pp. 234–241, Springer, 2015.
- [62] D. Gloudemans, G. Zachár, Y. Wang, J. Ji, M. Nice, M. Bunting, W. W. Barbour, J. Sprinkle, B. Piccoli, M. L. D. Monache, *et al.*, “So you think you can track?,” in *Proceedings of the IEEE/CVF Winter Conference on Applications of Computer Vision*, pp. 4528–4538, 2024.
- [63] C. Chen, K. Petty, A. Skabardonis, P. Varaiya, and Z. Jia, “Freeway performance measurement system: mining loop detector data,” *Transportation research record*, vol. 1748, no. 1, pp. 96–102, 2001.
- [64] Y. Zhang, M. Quinones-Grueiro, Z. Zhang, Y. Wang, W. Barbour, G. Biswas, and D. Work, “Marvel: Multi-agent reinforcement-learning for large-scale variable speed limits,” *arXiv preprint arXiv:2310.12359*, 2023.
- [65] A. Coursey, J. Ji, M. Quinones-Grueiro, W. Barbour, Y. Zhang, T. Derr, G. Biswas, and D. B. Work, “Ft-aed: Benchmark dataset for early freeway traffic anomalous event detection,” *arXiv preprint arXiv:2406.15283*, 2024.
- [66] S. Vallender, “Calculation of the wasserstein distance between probability distributions on the line,” *Theory of Probability & Its Applications*, vol. 18, no. 4, pp. 784–786, 1974.
- [67] N. Tsanakas, J. Ekström, and J. Olstam, “Generating virtual vehicle trajectories for the estimation of emissions and fuel consumption,” *Transportation Research Part C: Emerging Technologies*, vol. 138, p. 103615, 2022.